

PAPER

An n -body potential for a Zr–Nb system based on the embedded-atom method

To cite this article: De-Ye Lin *et al* 2013 *J. Phys.: Condens. Matter* **25** 105404

View the [article online](#) for updates and enhancements.

You may also like

- [Thermophysical properties and atomic structure of liquid Zr–Nb alloys investigated by electrostatic levitation and molecular dynamics simulation](#)
D D Zuo, J Chang, Q Wang et al.
- [Effects of Nb concentration and temperature on generalized stacking fault energy of Zr–Nb alloys by molecular dynamics simulations](#)
Hailian Wang, Rongjian Pan, Aitao Tang et al.
- [Atomistic simulations of the interaction of edge dislocations with -Nb precipitates in Zr–Nb alloys](#)
Junru Lin, Shuaijie Chen, Yiding Bai et al.

Corrigendum: An n -body potential for a Zr–Nb system based on the embedded-atom-method

2013 *J. Phys.: Condens. Matter* **25** 105404

De-Ye Lin¹, S S Wang¹, D L Peng¹, M Li² and X D Hui¹

¹ State Key Laboratory for Advanced Metals and Materials, University of Science and Technology Beijing, Beijing 100083, People's Republic of China

² Department of Materials Science and Engineering, Georgia Institute of Technology, Atlanta, GA 30332, USA

E-mail: xdhui@ustb.edu.cn

Received 4 April 2013

Published 19 April 2013

Online at stacks.iop.org/JPhysCM/25/209501

The authors regret that some errors occurred in the following parts of our article:

(1) For equations (6) and (7), the correct formulas must be:

$$F(\rho) = \sum_{i=0}^3 F n_i \left(\frac{\rho}{\rho_n} - 1 \right)^i, \quad \rho < \rho_n, \quad \rho_n = 0.85 \rho_e, \quad (1)$$

$$F(\rho) = \sum_{i=0}^3 F_i \left(\frac{\rho}{\rho_e} - 1 \right)^i, \quad \rho_n \leq \rho < \rho_o, \quad \rho_o = 1.15 \rho_e. \quad (2)$$

(2) In the main text, section 3.1, paragraph 2, line 11: 'It is seen that the cohesive energy, lattice constants, vacancy

formation energy and elastic constants reproduced for both Zr and Nb agree with those obtained by the first-principles calculations (for Zr: [43–45]; for Nb: [43, 44, 51–53]) and experimental data (for Zr: [23, 31, 39, 47–50]; for Nb: [31, 39, 46, 54, 55]) very well'. There is no [23] for Zr in experimental data, and the correct sentence must be: '... and experimental data (for Zr: [31, 39, 47–50] ...'.

(3) In table 4, the reference number for TB-SMA must be [30] (instead of [38]), and it should be left blank for E_{1v}^f in this column.

(4) In table 6, the reference number for TB-SMA must also be [30] (instead of [20]). This is a typographical error.

An n -body potential for a Zr–Nb system based on the embedded-atom method

De-Ye Lin¹, S S Wang¹, D L Peng¹, M Li² and X D Hui¹

¹ State Key Laboratory for Advanced Metals and Materials, University of Science and Technology Beijing, Beijing 100083, People's Republic of China

² Department of Materials Science and Engineering, Georgia Institute of Technology, Atlanta, GA 30332, USA

E-mail: xdhui@ustb.edu.cn

Received 17 September 2012, in final form 21 January 2013

Published 8 February 2013

Online at stacks.iop.org/JPhysCM/25/105404

Abstract

A novel n -body potential for an Zr–Nb system was developed in the framework of the embedded-atom method. All the parameters of the constructed potential have been systematically evaluated by fitting to the ground state properties obtained from experimental measurements and first-principles calculations for pure elements and some alloys. It is shown that most of the static thermodynamics properties for Zr and Nb can be well reproduced by using the present potential. Some calculation results based on the present model are even closer to the experimental data than those based on previous potential models. The ground state properties of hypothetical Zr–Nb alloys were also calculated and found to be in agreement with first-principles calculations. Furthermore, the formation energies of random solid solutions of Zr–Nb with lattices of body centered cubic (bcc) and hexagonal close packed (hcp) type were calculated by fitting the energy–volume relations to Rose's equation of state. These values were compared with those obtained by first-principles calculations based on special quasirandom structure models and the Miedema-ZSL-07 model (the improved Miedema model proposed by Zhang, Sheng and Liu in 2007). It is indicated that our n -body constructed potential for a Zr–Nb alloy provides an effective description for the interaction between the dissimilar ion interactions for hcp–bcc systems.

(Some figures may appear in colour only in the online journal)

1. Introduction

Zirconium has the advantages of very low thermal neutron absorption cross-section, high hardness, ductility and corrosion resistance. When alloyed with less than 2 wt% of niobium or some other metals, the mechanical properties and corrosion resistance of Zr-based alloys are remarkably improved [1]. Therefore, Zr-based alloys have been widely employed for the cladding of fuel rods and pressure tubes in nuclear reactors. For example [2], ZIRLO (Zr–1%Nb–1%Sn–0.1%Fe) [3] and M5 (Zr–1%Nb–O) [4] alloys have been used for the fuel cladding materials of pressurized water reactors, and Zr–2.5Nb alloy for the pressure tubes of heavy water reactors [5]. E110 (Zr–1%Nb) and E635 (Zr–1.3%Sn–1%Nb–0.4%Fe) alloys have been utilized in water cooled reactors for VVER and RMBK

cores [6]. Considering that all these alloys are mainly composed of Zr and Nb, it is intriguing to investigate the effects of Nb addition on the irradiation effects of the alloys. In particular, the evolution of displacement cascades generated by the transfer of energy from neutrons to the atomic system is critical to understanding the irradiation mechanism. Because the lifespan of whole displacement cascade process is only of several picoseconds, it is difficult to study these phenomena by experimental means [7]. Used as an alternative, molecular dynamics (MD) simulations have become a powerful tool for modeling irradiation effects [7–10].

A sound n -body potential is fundamental to the characterization of atomic structures and dynamics properties of condensed matter by MD methods. For n -body potentials, the widely used methods are in the framework of Finnis

and Sinclair potentials (FS potentials) [11, 12], the second-moment approximation of tight binding theory (TB-SMA) model [13], and the embedded-atom method (EAM) [14–16]. Generally speaking, the FS and EAM potentials are suitable for cubic transition metals, while TB-SMA potentials are more preferable for hcp and fcc metals [17]. When it comes to an hcp–bcc system like Zr–Nb, the description of the interatomic interactions between dissimilar atoms is still an undergoing issue.

To retain the transformation invariance of monatomic systems, Johnson *et al* [18] proposed a simple form of cross-potential based on EAM for alloys. This model has been widely used by several researchers [19–22]. From that time, Baskes and Lee *et al* [23–25] have developed a series of n -body potentials for transition metals based on the modified embedded-atom method (MEAM) by taking into account the directionality of bonding. However, Mishin *et al* [26, 27] pointed out that for MEAM, the angularly dependent interaction which constitutes a part of the tensor electron density is introduced through dipole, quadrupole and high-order multipole correction in the electron density function. That makes the computations of the energy and force using MEAM for a system, especially for a large one, cost much more time than those using FS, TB-SMA, and EAM. Besides, the cross-potential for an alloy system based on MEAM was constructed just based on a specific structure of one composition. This may yield the obvious deviation of calculated physical properties from those measured experimentally for different compositions [28]. To overcome this problem, Mishin *et al* developed an angularly dependent potential (ADP) [26] based on EAM, in which the directionality of bonding was moderately considered. By introducing the additional terms into non-central components of bonding, the solutions for the energy and force of ADP are simplified. It has been found that the simulation time based on this model is just approximately a factor of two longer than those for other EAM potentials [26]. Unfortunately, only a few potentials for bcc–fcc systems based on ADP have been reported at present [26, 27]. Zhang *et al* have constructed a series of n -body potentials for hcp–bcc metal systems based on the EAM model [17]. They adopted the EAM model for hcp elements developed by Cai [19] and the model for bcc elements developed by Johnson [16]. To combine the hcp–hcp and bcc–bcc potentials together, they employed the cross-potential suggested by Gong *et al* [29]. These treatments were found to cause some problems, e.g. the energy and force derived from the potential often have discontinuity at the cutoff radius, which may spoil the energy conservation and lead to unphysical phenomena in simulations [30]. Therefore, it is imperative to develop novel n -body potentials with smooth truncations for systems of interest.

As for the n -body potentials of Zr–Nb alloys, Li *et al* proposed an analytic formula based on the modified TB-SMA model. This model could reproduce some properties of Zr–Nb system rationally [30]. However, neither the point defects nor the surface energy had been considered properly, which greatly limited its applications. In this work, we aim to construct a sound n -body potential for Zr–Nb within the

framework of the EAM method. We employ the analytic formulas for pure Zr and Nb elements suggested by Wadley *et al* [20, 21]. All the parameters of the potentials of pure elements are optimized by fitting to the ground properties of Zr and Nb. The cross-potential for the Zr–Nb binary system is determined by fitting particular properties obtained from first-principles calculations to a cubic polynomial function. By using the constructed potential, the static properties and dynamic properties of Zr–Nb are reproduced and calculated. Furthermore, by using this potential, the formation energies for random solid solutions of Zr–Nb in bcc and hcp lattices are also calculated. It is believed that this work has implications for the development of n -body potentials for hcp–bcc binary systems.

2. The model and methodology

On the basis of the EAM theory, the total energy of a system can be calculated by using

$$E_{\text{total}} = \sum_i F(\rho_i) + \frac{1}{2} \sum_{j \neq i} \phi(r_{ij}) \quad (1)$$

$$\rho_i = \sum_j \varphi(r_{ij}) \quad (2)$$

where r_{ij} is the distance between atoms i and j , ρ_i is the total electron density at the atom i site due to all other atoms, and $F(\rho_i)$ is the embedding energy which represents the n -body contributions. $\phi(r_{ij})$ is the two-body repulsive potential, and $\varphi(r_{ij})$ is the electron density distribution function. The integrations are over all the neighbors of i atom within the cutoff radii.

In this work, we employ Wadley's EAM potential to construct the potentials of pure elements [20, 21], which results in a natural cutoff procedure and has been proved to be valid for bcc, fcc and hcp transition metals. The pair potential function and electron density distribution function can be expressed as

$$\phi(r_{ij}) = \frac{A \exp[-\alpha(r_{ij}/r_e - 1)]}{[1 + (r_{ij}/r_e - \kappa)^m]} - \frac{B \exp[-\beta(r_{ij}/r_e - 1)]}{[1 + (r_{ij}/r_e - \lambda)^n]} \quad (3)$$

$$\varphi(r_{ij}) = \frac{f_e \exp[-\beta(r_{ij}/r_e - 1)]}{[1 + (r_{ij}/r_e - \lambda)^n]} \quad (4)$$

where A , B , α , β , m , n , κ , λ and f_e are potential parameters. As suggested in [20], the values of m and n could be set directly as 20, providing natural cutoff distances for the potentials that are controlled by parameters κ and λ . f_e can also be defined as Wadley *et al* did [20]:

$$f_e = \frac{E_c}{\Omega^{1/3}} \quad (5)$$

where E_c is the cohesive energy and Ω is the atomic volume.

As Wadley *et al* pointed out [20], though the standard embedding function $F(\rho)$ adopted by Johnson *et al* [14–16] could produce physically reasonable results at the equilibrium state ($\rho = \rho_e$), this formula still has two main disadvantages

in physics: (1) the embedding function $F(\rho)$ approaches zero with infinite slope at $\rho = 0$; (2) the pressure derivatives of the bulk modulus $((\partial B/\partial p)|_{T=0})$ are always in the range 4–5 for metals while the standard function gives either much larger or smaller results with seemingly no systematic variation. Therefore, a set of new embedding functions were introduced to overcome these disadvantages:

$$F(\rho) = \sum_{i=0}^3 F_{n_i} \left(\frac{\rho}{\rho_n} \right)^i, \quad \rho < \rho_n, \quad \rho_n = 0.85\rho_e \quad (6)$$

$$F(\rho) = \sum_{i=0}^3 F_i \left(\frac{\rho}{\rho_e} \right)^i, \quad \rho_n \leq \rho < \rho_0, \quad \rho_0 = 1.15\rho_e \quad (7)$$

$$F(\rho) = F_e \left[1 - \ln \left(\frac{\rho}{\rho_e} \right)^\eta \right] \left(\frac{\rho}{\rho_e} \right)^\eta, \quad \rho \geq \rho_0 \quad (8)$$

where ρ_e is the equilibrium electron density, and F_{n_i} , F_i , F_e and η are the parameters of embedding functions. As shown in equation (6), a simple cubic function was introduced to ensure that $F(\rho)$ and its first derivative would give the zero value at $\rho = 0$. Another cubic function as equation (7) was also adopted in the near equilibrium state range $\rho \in [0.85\rho_e, 1.15\rho_e]$. The function was fitted to some basic physical properties from experimental data, such as the lattice constant, cohesive energy, vacancy formation energy, elastic constants and $(\partial B/\partial p)|_{T=0}$ for Zr and Nb, together with the pair potential and electron density function. The values of $(\partial B/\partial p)|_{T=0}$ were calculated from a universal equation of state proposed by Rose *et al* [31]; they are 4.43 and 4.10 for Zr and Nb, respectively. Since the standard embedding function is valid at large ρ , it works as equation (8) when $\rho \geq \rho_0$. By fitting the value, slope and concavity of these embedding functions at $\rho = 0$, $\rho = 0.85\rho_e$ and $\rho = 1.15\rho_e$, the smooth embedding functions that match appropriate physical criteria in all cases could be obtained (more information can be found in [20]).

Once the analytic formulas for the electron density function, pair potential function and embedding functions have been defined, the parameters for pure elements are determined by fitting some basic physical properties from experimental data for Zr and Nb. In the fitting process, the pressure derivative of the bulk modulus is also included, which takes the value calculated from a universal equation of state proposed by Rose *et al* [31]. Besides this, $\frac{dE}{da}|_{a=a_0} = 0$ and $\frac{d^2E}{da^2}|_{a=a_0} > 0$ have been treated as two additional conditions to keep the physical rationality. For the hcp structure, it is difficult to satisfy the requirement of zero stress-tensor diagonal components (σ_{11} and σ_{33}) under the equilibrium state simultaneously for anisotropy. As Willaime *et al* suggested [32], the stress-tensor diagonal components $\sigma_{ij} = 0$ are not necessary in a non-cubic structure. Instead, to maintain the stability of the hcp lattice, the absolute values of σ_{ij} for hcp Zr are restricted to being lower than 0.05 kbar in the whole fitting process.

To determine the Zr–Nb cross-potential, a ten-piece cubic polynomial function (equation (9)) is introduced to fit enough

alloys with different structures over a wide composition range:

$$\phi(r_{ij}) = \sum_{k=1}^{10} A_k (x_k - r)^3 H(x_k - r) \quad (9)$$

where $H(x)$ is the Heaviside step function, the x_k knots are determined by careful choosing in the cutoff radius range, and the A_k are the additional parameters of the potential.

For the Zr–Nb system, few intermetallic compounds have been reported under an equilibrium state. It is not possible to fit the cross-potential of Zr–Nb directly by using experimental data. Therefore, the first-principles method, which has already been proved to be a reliable way to predict some physical properties of the alloys, was introduced to assist the construction of the Zr–Nb cross-potential. In this work, several hypothetical alloys with different structures ($B1$, $B2$, $B3$, $B8_1$, $C1$, $C3$, $C7$, $C15$, $C32$, C_h , $D0_3$, $D0_9$, $D0_{19}$ and $L1_2$ structures) were created and calculated by the first-principles method. The first-principles calculations were conducted by using VASP [33]. In these calculations, the projector augmented wave (PAW) [34] method and ultrasoft pseudopotentials [35] were employed. The exchange and correlation functional was described by using the generalized-gradient approximation, with the PW91 functional [36]. The integration in the Brillouin zone was done by using enough points in the mesh determined by the Monkhorst–Pack scheme [37] and a moderate cutoff energy was introduced to ensure that the absolute energy is converged to less than 0.1 meV/atom. By fitting particular properties (cohesive energies and lattice constants) of Zr–Nb on the basis of first-principles calculations, the parameters of the Zr–Nb cross-potential were determined.

To test the validity of the constructed potential, molecular dynamics simulations were performed by using LAMMPS³ [38]. For most of the calculations in this work, the sizes of the calculated systems were defined as follows: for the hcp structure, the x , y and z axes are along the $[1\ 0\ 0]$, $[0\ \sqrt{3}\ 0]$ and $[0\ 0\ c/a]$ crystal directions; for the bcc structure, the x , y and z axes are along the $[1\ 0\ 0]$, $[0\ 1\ 0]$ and $[0\ 0\ 1]$ crystal directions. When it comes to the calculations of surface formation energies and stacking fault energies, the x , y and z direction were determined according to the index of surfaces of interest. For example, to calculate the (110) surface formation energy of Nb, a bcc lattice was created, in which the x axis is along $[1\ 1\ 0]$, the y axis is along $[\bar{1}\ 1\ 0]$, and the z axis is along $[0\ 0\ 1]$, while to calculate the $(1\ \bar{1}\ 0\ 0)$ surface formation energy of Zr, an hcp lattice was created, in which the x axis is along $[1/2\ -\sqrt{3}/2\ 0]$, the y axis is along $[0\ 0\ c/a]$, and the z axis is along $[-\sqrt{3}/2\ 1/2\ 0]$. A 15 Å thick vacuum slab was introduced in the z direction to ensure that the interactions between the nearest free surfaces are negligible. The basic unit cells used to create these boxes were determined according to the experimental crystal information for Zr and Nb, where $a = 3.2316$, $c/a = 1.5929$ for Zr and $a = 3.3004$ for Nb [39]. All of the boxes used in this work are listed in table 1. A real system always has

³ LAMMPS Molecular Dynamics Simulator <http://lammps.sandia.gov>.

Table 1. The size of the calculated boxes for Zr and Nb in this work. In the calculations of the surface formation energies and stacking fault energies, a 15 Å thick vacuum slab has been introduced in the z direction to ensure that the interactions between the nearest free surfaces constructed are negligible.

			Zr	
Calculations			Box scale	Box length (Å × Å × Å)
Point defects			10 × 10 × 10	32.316 × 55.973 × 51.476
Surface energies	(0001)		20 × 20 × 10	64.632 × 64.632 × 63.902
	(1100)		20 × 20 × 10	64.632 × 102.952 × 41.121
	(1120)		20 × 20 × 10	102.952 × 111.946 × 29.542
Stacking fault energies (0001)	I1		20 × 20 × 10	64.632 × 64.632 × 63.902
	I2		20 × 20 × 10	64.632 × 64.632 × 63.902
	E		20 × 20 × 10	64.632 × 64.632 × 63.902
Any other calculations if not stated otherwise			10 × 10 × 10	32.316 × 55.973 × 51.4762
			Nb	
			Box scale	Box length (Å × Å × Å)
Point defects			10 × 10 × 10	30.004 × 30.004 × 30.004
Surface energies	(110)		20 × 20 × 10	93.349 × 66.008 × 36.004
	(100)		20 × 20 × 10	66.008 × 66.008 × 46.354
	(111)		20 × 20 × 10	93.349 × 93.349 × 33.102
Stacking fault energies (γ surfaces)	{110}		20 × 20 × 20	93.349 × 66.008 × 93.349
	{112}		20 × 20 × 20	93.349 × 114.329 × 161.686
Any other calculations if not stated otherwise			10 × 10 × 10	30.004 × 30.004 × 30.004

atoms at a magnitude above $\sim 10^{23}$, so periodic boundary conditions were also adopted in all three directions. All of the calculations were carried out under the *NPT* ensemble, which allows the size of the simulation box to change. The external pressure was set to zero and the temperature was controlled using the N se–Hoover thermostat method [40, 41]. The equation of motion was solved by using a velocity Verlet integrator with a time step of 1 fs. For pure elements, the thermal expansion coefficient for the range 273–373 K, heat of fusion, melting point, specific heat capacity, point defects, and formation energies of surface and stacking faults were calculated on the basis of the constructed potential. The cohesive energy, lattice constants and bulk modulus of hypothetical alloys and the formation energies of random solid solutions with hcp and bcc structure were also calculated.

3. Results and discussion

3.1. Basic physical properties and lattice stability

By using the above described modeling strategy, we developed a new n -body potential for the Zr–Nb system. Since there are many parameters and properties involved in the fitting, a weighted least squares algorithm has been introduced in order to obtain a set of the most optimized parameters. The cohesive energy, lattice constants, vacancy formation energy, and first derivative of the bulk modulus were fitted with high weight (1.0), and the elastic constants and bulk modulus were fitted with low weight (0.1). By using a computer code written by the authors' group for fitting the n -body potentials, all of the undetermined parameters were fully optimized by minimizing the weighted mean squared deviation of the aforementioned target properties simultaneously. Under the condition that the cutoff radii of the pair potential and electron

density function were both set to 7.0 Å, all the parameters of the new potential were fitted and they are listed in table 2. To verify the reliability of the constructed potential, some basic physical properties of Zr and Nb were reproduced; these are listed in table 3 and 4, respectively.

For comparison, the results of first-principles calculations and experimental measurements from previous work were also presented. To make the references more systematic and clear, the MEAM potentials referenced in this work are marked as follows. For Zr, the potentials developed by Baskes *et al* [23] and Kim *et al* [42] are marked as MEAM-Baskes and MEAM-Kim; for Nb, the potentials developed by Baskes *et al* [46] and Lee *et al* [24] are marked as MEAM-1NN-Baskes (only the contributions of first-nearest neighbors have been considered) and MEAM-2NN-Lee (the second-nearest neighbors have also been included). It is seen that the cohesive energy, lattice constants, vacancy formation energy and elastic constants reproduced for both Zr and Nb agree with those obtained by the first-principles calculations (for Zr: [43–45]; for Nb: [43, 44, 51–53]) and experimental data (for Zr: [23, 31, 39, 47–50]; for Nb: [31, 39, 46, 54, 55]) very well. Comparing with the MEAM-Kim model [42], the lattice constants of Zr reproduced by the present model are reasonable, although no angularly dependent force distribution has been considered. The c/a ratio is close to that obtained by first-principles calculation [43], and the lattice constant (a) is a little bit underestimated—about 0.40%. It is also noticed that the values of $(\partial B/\partial p)|_{T=0}$ for both Zr and Nb could be reproduced exactly as expected.

It is very important for a potential to avoid lattice instabilities in the calculations. In this work, we have calculated the energy differences (ΔE) between referenced structures and some hypothetical structures, such as the ideal hcp, face centered cubic (fcc), body centered cubic (bcc),

Table 2. The fitted EAM parameters for the Zr–Nb system.

Zr		Nb		Zr–Nb	
m	20	m	20	x_1	3.0
n	20	n	20	x_2	3.4
r_e	3.178 925	r_e	2.858 230	x_3	3.8
f_e	2.188 934	f_e	2.889 832	x_4	4.2
ρ_e	29.898 100	ρ_e	31.744 900	x_5	4.6
ρ_s	29.898 100	ρ_s	31.744 900	x_6	5.0
α	8.004 031	α	7.514 546	x_7	5.4
β	4.268 817	β	4.500 000	x_8	5.8
A	0.428 969	A	0.569 650	x_9	6.4
B	0.607 804	B	0.905 874	x_{10}	7.0
κ	0.5	κ	0.136 112	A_1	1.317 398
λ	1.0	λ	0.388 893	A_2	−0.921 792
Fn_0	−4.515 573	Fn_0	−4.928 550	A_3	1.068 635
Fn_1	−0.383 438	Fn_1	−0.549 044	A_4	0.068 854
Fn_2	1.182 951	Fn_2	1.680 064	A_5	−0.545 070
Fn_3	−2.949 184	Fn_3	−2.699 442	A_6	0.504 415
F_0	−4.548 461	F_0	−4.975 703	A_7	−0.252 223
F_1	0.0	F_1	0.0	A_8	0.093 271
F_2	1.377 717	F_2	1.980 875	A_9	−0.060 200
F_3	−0.559 833	F_3	−0.765 504	A_{10}	0.017 314
η	0.780 469	η	0.890 133		
F_e	−4.548 462	F_e	−4.975 568		

Table 3. The static properties of Zr reproduced by the present model and other models, first-principles calculations and their comparisons with experimental data. For E_{lv}^f , the result calculated by the first-principles calculation is the unrelaxed value. For $(\partial B/\partial p)|_{T=0}$ in the experimental measurement, the first line is derived by using the Rose equation of state [31].

	FS [12]	TB-SMA [30]	MEAM-Kim [42]	First-principles calculations	This work	Experiment
E_c (eV)	6.25	6.19	6.36		6.25	6.25 [47]
a (Å)	3.249	3.18	3.231	3.230 [43]	3.2171	3.2316 [39]
c/a	1.597	1.632	1.5862	1.606 [43]	1.6046	1.5929 [39]
C_{11} (GPa)	150	142	151.5	145.3 [44]	128.3	143.4 [39]
C_{12} (GPa)	85	67.0	71.8	67.3 [44]	74.4	72.8 [39]
C_{44} (GPa)	36	26.0	34.1	24.3 [44]	29.0	32.0 [39]
C_{13} (GPa)	67	55.0	66.1	69.5 [44]	79.7	65.3 [39]
C_{33} (GPa)	175	154	160.6	166.1 [44]	180.9	164.8 [39]
B_0 (GPa)		89.0	96.8	95.3 [44]	100.5	95.4 [48]
$(\partial B/\partial p) _{T=0}$				3.44 [44]	4.43	4.43 [31]
E_{lv}^f (eV)		2.13	2.09	2.07 [45]	1.79	1.70 [49] 1.74 [50]

Table 4. The static properties of Nb reproduced by the present model and other models, first-principles calculations and their comparisons with experimental data. For $(\partial B/\partial p)|_{T=0}$ in the experimental measurement, the first line is derived by using the Rose equation of state, and the second line gives the experimental data [31].

	FS [11]	TB-SMA [38]	MEAM-2NN-Lee [24]	First-principles calculations	This work	Experiment
E_c (eV)	7.57	7.57	7.47		7.57	7.57 [47]
a (Å)	3.3008	3.30	3.3024	3.322 [43]	3.3000	3.3004 [39]
C_{11} (GPa)	246.6	247	252.7	247.2 [44]	262.2	246.5 [39]
C_{12} (GPa)	133.2	135	133.1	140.0 [44]	124.6	134.5 [39]
C_{44} (GPa)	28.1	29.0	31.9	14.2 [44]	35.95	28.73 [39]
B_0 (GPa)	171.0	172	173.0	172.3 [44]	170.2	170.2 [39]
$(\partial B/\partial p) _{T=0}$			4.23	3.89 [44]	4.10	4.10 [31] 4.72 [31]
E_{lv}^f (eV)	2.64	2.64	2.75	2.92 [51] 2.32 [52] 2.79–2.88 [53]	2.75	2.75 [46] 2.7 [55]

simple cubic (sc) and diamond structures, as listed in tables 5 and 6. The referenced structures are the corresponding hcp and bcc equilibrium structures for Zr and Nb. For comparison,

the results calculated by using other models of Zr and Nb are also listed. From table 5, it is seen that for the hcp \rightarrow ideal hcp structural transition of Zr, the calculated

Table 5. The structural energy differences ΔE (eV/atom) for Zr calculated by using the present model, TB-SMA [30], MEAM-Baskes [23], MEAM-Kim [42], and the first-principles calculations [43]. a_s (Å) is the corresponding lattice constant of the specific structure.

		Zr	
		a_s	ΔE
$\Delta E_{\text{hcp} \rightarrow \text{ideal hcp}}$	This work	3.202	0.0007
	MEAM-Baskes		0.0105
$\Delta E_{\text{hcp} \rightarrow \text{fcc}}$	This work	4.537	0.010
	TB-SMA	4.49	0.00
	MEAM-Baskes		0.017
	MEAM-Kim		0.055
$\Delta E_{\text{hcp} \rightarrow \text{bcc}}$	First-principles calculation	4.529	0.0382
	This work	3.588	0.009
	TB-SMA	3.57	0.04
	MEAM-Baskes		0.061
	MEAM-Kim	3.580	0.019
$\Delta E_{\text{hcp} \rightarrow \text{sc}}$	First-principles calculation	3.574	0.0756
	This work	2.965	0.54
$\Delta E_{\text{hcp} \rightarrow \text{diamond}}$	MEAM-Baskes		0.45
	This work	6.438	1.40
	MEAM-Baskes		1.48

$\Delta E_{\text{hcp} \rightarrow \text{ideal hcp}}$ is smaller than that from MEAM-Baskes [23]. Although the angularly dependent force contribution of hcp Zr has not been considered, the $\Delta E_{\text{hcp} \rightarrow \text{ideal hcp}}$ value is large enough to ensure that ideal hcp is not the most stable phase for Zr at 0 K. For the hcp \rightarrow fcc structural transition, the calculated $\Delta E_{\text{hcp} \rightarrow \text{fcc}}$ from the present model is comparable with that from MEAM-Baskes [23], but smaller than those from MEAM-Kim [42] and first-principles calculations [43]. The lattice constant reproduced agrees with that obtained by the first-principles calculation well. It is seen that the hcp and fcc structures cannot be distinguished properly using the TB-SMA model [30]. Although the constructed potential somewhat underestimates $\Delta E_{\text{hcp} \rightarrow \text{bcc}}$, the bcc lattice constant reproduced agrees with that from MEAM-Kim [42] and first-principles calculation [43] very well. It is also shown that $\Delta E_{\text{hcp} \rightarrow \text{sc}}$, $\Delta E_{\text{hcp} \rightarrow \text{diamond}}$ and the corresponding lattice constants based on this model are also consistent with those from the first-principles method and MEAM-Baskes model [23]. Therefore, it can be concluded that although it presents some deviations in the energy difference calculations compared with previous work and the first-principles calculations, the constructed potential could ensure that the hcp structure has the lowest potential energy among the calculated structures, i.e., the hcp structure is the equilibrium state of Zr at room temperature. For Nb, it is found from table 6 that the calculated structural energy differences and lattice constants are comparable with those from MEAM-2NN-Lee [24], TB-SMA [30] and first-principles calculations [43]. All these results indicate that the lattice stability of pure elements reproduced by the present model is reasonable.

Because all the parameters were fitted using the basic properties under the equilibrium state, the validity of the constructed potential should be tested beyond the equilibrium

Table 6. The structural energy differences ΔE (eV/atom) for Nb calculated by using the present model, TB-SMA [20], MEAM-2NN-Lee [24], and the first-principles calculations [43]. a_s (Å) is the corresponding lattice constant of the specific structure.

		Nb	
		a_s	ΔE
$\Delta E_{\text{bcc} \rightarrow \text{ideal hcp}}$	This work	2.937	0.240
	TB-SMA	2.84	0.21
	MEAM-2NN-Lee	2.947	0.164
	First-principles calculation	2.880	0.2915
$\Delta E_{\text{bcc} \rightarrow \text{fcc}}$	This work	4.154	0.240
	TB-SMA	4.04	0.22
	MEAM-2NN-Lee	4.169	0.176
	First-principles calculation	4.230	0.3234
$\Delta E_{\text{bcc} \rightarrow \text{sc}}$	This work	2.568	0.54
	MEAM-2NN-Lee	2.606	0.90
$\Delta E_{\text{bcc} \rightarrow \text{diamond}}$	This work	5.415	2.05
	MEAM-2NN-Lee	5.425	1.44

state. Rose *et al* proposed a universal equation of state (EOS) for solid materials [31], which could reproduce well the relationship of energy versus volume under moderate compressions and expansions for transition metals. To verify the transferability of the constructed potential, we deduced the energy–distance (the nearest distance) relationship based on the present model, and compared it with the EOS. The relationship between the pressure and volume derived from the present model is shown in figure 1. As shown in figure 1, both the EOSs for Zr and Nb derived from the constructed potential are in reasonably good agreement with Rose’s EOS. It is also found that the pressure–volume relation derived from the present model agrees with that from the EOS very well even under large compressions ($0.3 < V/V_0 < 1.0$). These results indicate that the potential is valid for describing the state beyond equilibrium, although no metastable properties were included in the fitting process. In addition, it is seen that the potential exhibits a smooth cutoff for both energy and force, avoiding the unphysical behaviors in MD simulations due to the jumps at the radii without a proper truncation treatment.

3.2. Point defect calculations

Because the constructed potential is expected to apply for the simulation of irradiation damage, it is important to test its validity in the description of defects. By using the constructed potential, the monovacancy formation energy (E_{1v}^f), vacancy migration energy (E_{1m}), activation energy for self-diffusion by the vacancy mechanism (Q_{1m}), formation energy (E_{2v}^f) and binding energy (E_{2v}^b) of the divacancy were calculated through MD simulation with LAMMPS.

The vacancy migration energy is the energy difference between one atom at the saddle point and its equilibrium site as it moves from one crystal site to the nearest vacant site. In this work it was calculated with the following strategy. Firstly, to make sure that the neighbor vacancies have negligible influences on the vacancy or divacancy calculations, a large enough unit cell ($10 \times 10 \times 10 \times 4 = 4000$ atoms for Zr,

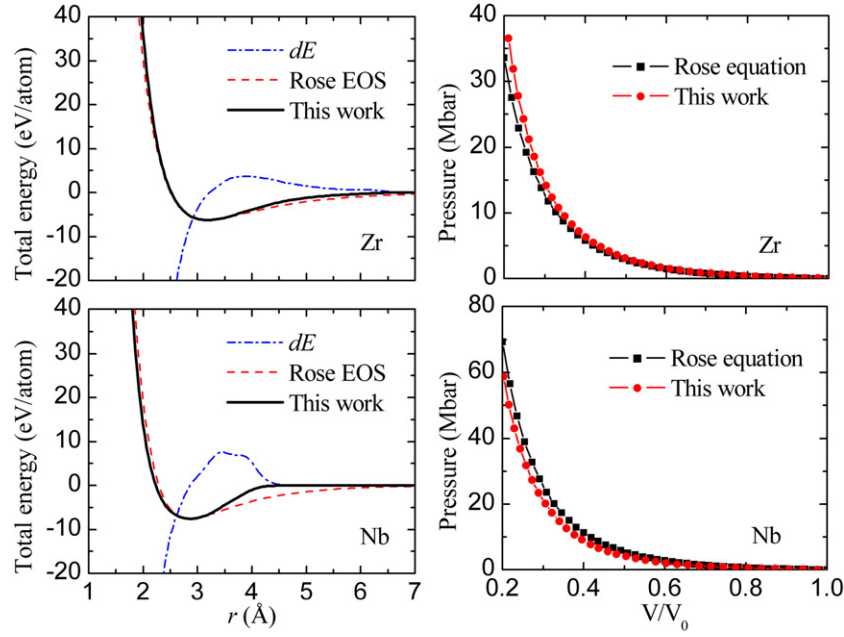


Figure 1. The total energies and their first derivatives as a function of the nearest-neighbor distance for Zr and Nb calculated from the present model compared with results from Rose *et al* [31].

$10 \times 10 \times 10 \times 10 = 2000$ atoms for Nb) was constructed. Then one or two vacancies were generated in the center of the box. The energies for an atom at different points (21 points in this work) along the moving paths from the original vacant site to the nearest vacant site were calculated. By subtracting the energy at the equilibrium site, a series of E_{1m} were obtained. To find the exact saddle point, we fitted these energies with a sixth-order polynomial function. The corresponding energy is called the vacancy migration energy. For hcp Zr, there are two favorable paths for the vacancy migration, i.e. two different saddle points. The migration energies are correspondingly expressed as E_{1m}^{in} and E_{1m}^{out} for the atom which moves in and out of the basal plane, respectively. The calculated results and their fitted curves of E_{1m}^{in} and E_{1m}^{out} for Zr and Nb are shown in figure 3.

As the E_{1v}^f and E_{1m} were determined, the corresponding activation energy for self-diffusion Q_{1m} could be calculated by using

$$Q_{1m} = E_{1m} + E_{1v}^f. \quad (10)$$

Then the divacancy binding energy is obtained by using

$$E_{2v}^b = 2E_{1v}^f - E_{2v}^f. \quad (11)$$

All the calculated results are listed in tables 7 and 8. It is shown that the E_{1v}^f and E_{1m} for Zr are in good agreement with those from the analytic modified embedded-atom method (AMEAM) [56] and experiments [49, 50, 57–60]. The divacancy properties calculated by using our model are somewhat smaller than those from MEAM-Kim [42] and AMEAM [56]. Although the MEAM-Kim model can reproduce most of the basic physical properties well, as shown in table 3, this model obviously overestimated the vacancy formation energy and other point defect properties.

Table 7. The calculated point defect properties (in eV) for Zr based on the present model, and their comparisons with the work of others and experimental data.

	MEAM-Baskes [23]	MEAM-Kim [42]	AMEAM [56]	This work	Experiment
E_{1v}^f	1.93	2.09	1.70	1.79	1.70 [49] 1.74 [50]
E_{1m}^{out}		0.89	0.67	0.61	0.6–0.7 [57]
Q_{1m}^{out}		2.98	2.37	2.40	
E_{1m}^{in}		1.14	0.72	0.66	0.54–0.62 [58, 59]
Q_{1m}^{in}		3.23	2.42	2.45	3.17 [60]
E_{2v}^f (FN)		4.59	3.18	3.46	
E_{2v}^b (FN)	−0.53	0.41	0.21	0.12	
E_{2v}^f (SN)		4.55	3.18	3.45	
E_{2v}^b (SN)	−0.52	0.37	0.22	0.13	

For the divacancy calculations, the present model, like AMEAM [56] and MEAM-Kim [42], gives positive binding energies for the divacancy, indicating that the configurations of first-nearest (FN) and second-nearest (SN) divacancies are stable under these models. For MEAM-Baskes [23], negative values were obtained, indicating that the divacancy configurations are unstable on the basis of that model. This is obviously unreasonable. As for Nb, it is found that the results calculated by using the present model agree with those from MEAM-2NN-Lee [24], AMEAM [61] and experimental measurements very well [46, 54, 55, 62].

To examine the size effects on point defect calculations, a series of monovacancy and divacancy formation energies were

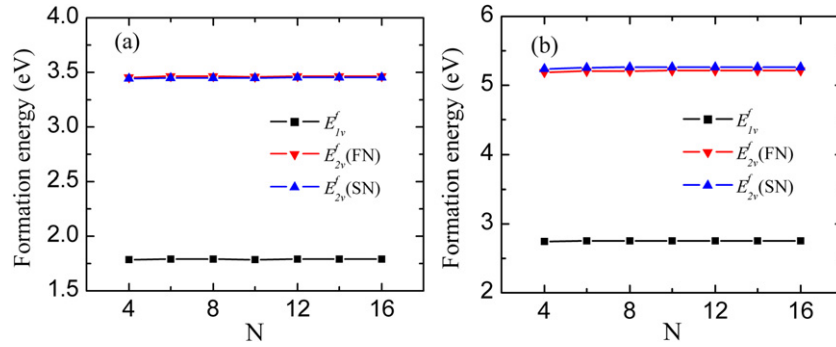


Figure 2. The formation energies of the monovacancy and divacancy calculated by using the present model for different sizes of boxes. Here N is the number of replications along the x , y and z axes of the calculated unit cells. (a) Zr; (b) Nb.

Table 8. The calculated point defect properties (in eV) for Nb based on the present model, and their comparisons with the work of others and experimental data. E_{1m} for MEAM was calculated with E_{1v}^f and Q_{1m} by using equation (10).

	MEAM-2NN- Lee [24]	AMEAM [61]	This work	Experiment
E_{1v}^f	2.75	2.76	2.75	2.75 [46] 2.7 [55]
E_{1m}	0.57	0.64	0.67	0.55 [55]
Q_{1m}	3.32	3.40	3.43	3.6 [62] 3.7 [54]
E_{2v}^f (FN)		5.16	5.21	
E_{2v}^b (FN)		0.36	0.29	
E_{2v}^f (SN)		5.20	5.26	
E_{2v}^b (SN)		0.32	0.24	

also calculated with different sizes of boxes and the results are displayed in figure 2. As shown in figure 2, the predicted formation energies for the monovacancy and divacancy are steady for both Zr and Nb as the supercell is larger than $8 \times 8 \times 8$. Thus it can be concluded that the size of the boxes in this work is moderate.

3.3. Surface and stacking fault formation energies

The formation energies of some low-index surfaces (E_{surf}) calculated by using the present model are listed in table 9. In the calculation, the box consists of $20 \times 20 \times 10 \times 2 = 8000$ atoms for both Zr and Nb, respectively. The vacuum slabs with the thickness of 15 Å along the corresponding surface directions were introduced so that the periodic surfaces have negligible influence on each other. For Zr, the formation energies of three typical surface were calculated: one basal plane (0001) and two prism planes ($1\bar{1}00$) and ($11\bar{2}0$). For the hcp metals with the c/a ratio below the ideal value like Zr, the corresponding density of the surface atom of the basal plane is higher than that of the prism plane. Therefore, a lower E_{surf} of the basal plane must be attained compared with those of prism planes. As shown in table 9, the surface formation energies of Zr calculated by using the constructed potential are somewhat lower than the experimental data [49, 63], but better than those from AMEAM [56]. The calculated surface formation energies of Zr have an order as follows: $E_{\text{surf}}(0001) < E_{\text{surf}}(1\bar{1}00) < E_{\text{surf}}(11\bar{2}0)$, which is consistent with results obtained from FS [12], MEAM-Baskes [23] and MEAM-Kim [42]. However, a contradictory result was

attained from the AMEAM model [56]. When it comes to Nb, the formation energies of (100), (110) and (111) surfaces were calculated. As table 9 shows, the formation energies of Nb calculated in this work are close to those from most other models [24, 30, 46, 61] and experimental data [24, 64]. For AMEAM [61], E_{surf} was underestimated again. Besides, compared with the results for the three low-index surface energies, an order as follows: $E_{\text{surf}}(110) < E_{\text{surf}}(100) < E_{\text{surf}}(111)$ was obtained, which is also in good agreement with experimental information [65, 66] as mentioned for MEAM-2NN-Lee [24].

The formation of stacking faults is an important deformation mechanism in metallic materials. For hcp metals, the formation energies of three typical basal plane stacking faults were calculated: i.e. growth fault (I1, ABAB|CBCB), deformation fault (I2, ABAB|CACA), both of which are intrinsic, and extrinsic fault (E, ABAB|C|ABAB) [67]. The calculated configurations were constructed on the basis of the (0001) configuration which was used in surface formation energy calculations. The stacking fault formation energies (E_{sf}) predicted from the present model and their comparison with those from other models and experiments are shown in table 10. For most models, only E_{sf} for I2 was calculated. As shown in table 10, E_{sf} calculated by using present model is larger than that from AMEAM [56], but smaller than those from other models. Most of these models underestimate E_{sf} greatly, compared with the values from the first-principles calculation [68] and experimental data [69], except for MEAM-Kim [42]. Nevertheless, it is found that the calculated E_{sf} has a relation as follows:

Table 9. The surface energies (mJ m^{-2}) calculated by using the present model and other models, and their comparisons with experimental data.

Zr	This work	FS [12]	MEAM-Baskes [23]	MEAM-Kim [42]	AMEAM [56]	Experiment
(0001)	1268	1022	2302	2156	988	2000 [49]
(1 $\bar{1}$ 00)	1353	1086	2364	2158	978	2050 [63]
(11 $\bar{2}$ 0)	1510	1230		2380		
Average	1377	1113	2333	2231	983	2025
Nb	This work	TB-SMA [30]	MEAM-1NN-Baskes [46]	MEAM-2NN-Lee [24]	AMEAM [61]	Experiment
(110)	1893	1792	1868	2490	1726	
(100)	2285	2101	2788	2715	1930	
(111)	2628	2343	2018	2923		
Average	2269	2079	2225	2709	1828	2300 [24] 2983 [64]

Table 10. The stacking fault energies (E_{sf}) of Zr calculated by using the present model and other models, and their comparisons with experimental data.

	E_{sf} (mJ m^{-2})		
	I1	I2	E
This work	21	43	64
FS [12]	41	80	118
MEAM-Baskes [23]		62	
MEAM-Kim [42]		201	
AMEAM [56]	13	26	40
First-principles calculations [68]		223	
Experimental [69]		340	
LREP [70]	56	84	166

$E_{\text{sf}}(\text{E}) \approx (3/2)E_{\text{sf}}(\text{I2}) \approx 3E_{\text{sf}}(\text{I1})$, which is in good agreement with those from FS [12], AMEAM [56], and the long range empirical potential (LREP) [70].

For bcc metals like Nb, the dissociation of dislocations into well-defined partial dislocations has not been observed directly experimentally, and the metastable stacking faults cannot be identified from such dissociation. Thus, γ surface calculations have been applied in most theoretical approaches to search for possible stacking faults of bcc metals [71–74]. In the calculation, a generalized stacking fault is created by displacing the top half of a crystal in a specific low-index plane along some crystallographic directions, and the crystal is assumed to be perfect on each side of the fault plane [72]. With increasing movement, a series of energies could be recorded, and this forms the so-called γ surface. The minima on the γ surface determine the possible metastable stacking faults. In this work, the sections through {110} and {112} γ surfaces in the $\langle 111 \rangle$ direction of Nb were calculated, where the screw dislocation Burgers vector $\mathbf{b} = (a_0/2)\langle 111 \rangle$ and a_0 is the lattice constant. At first, a $20 \times 20 \times 20$ bcc box was created. For the {110} calculation, the x , y and z axes of the box are along the [110], [001] and [1 $\bar{1}$ 0] directions; for the {112} calculation, the x , y and z axes of the box are along the [1 $\bar{1}$ 0], [1 $\bar{1}$ 1] and [1 $\bar{1}$ 2] directions. Thus, we have $20 \times 2 = 40$ layers and $20 \times 6 = 120$ layers in the supercells for {110} and {112} γ surface calculations, respectively. As is shown in the work of Fellingner *et al* [74], the differences between relaxed and unrelaxed calculations are very small;

thus only the unrelaxed γ surface energies were calculated. Results for generalized stacking fault energies calculated by using the present model and other models are displayed in figure 4. Comparing with the results from EAM based on the force-matched method and first-principles calculations by Fellingner *et al* [74], the γ surface sections in the $\langle 111 \rangle$ direction are somewhat underestimated in the present model. However, no minima on the γ surface have been found for either {110} or {112} calculations, which indicates that there are no stable stacking faults in the {110} and {112} planes along $\langle 111 \rangle$ directions. That is consistent with EAM and first-principles calculations. The same tendency was also found by previous work for some other bcc metals [72, 73, 75].

3.4. Thermal expansion and melting calculations

In this work, the thermodynamics properties including the thermal expansion coefficient, specific heat capacity, heat of fusion, and melting point have been calculated through MD simulations for a special system to further test the validity of the n -body constructed potential.

To calculate the thermal expansion coefficient, we first performed the MD simulation at 173 K for 200 ps to get a really stable state as an initial configuration. Then the box was continuously heated following a stepwise scheme from 173 K to 373 K with the temperature step 20 K. At each temperature the volume of the box was equilibrated for 200 ps and heated to the next temperature for 200 ps, resulting in the average heating rate of $5 \times 10^{10} \text{ K s}^{-1}$. The enthalpy, lattice constant and volume averages were determined over the last 100 ps. At low temperature, the temperature dependence of the lattice constant is almost linear. Therefore, we fitted the data from 273 K to 373 K to estimate the thermal expansion coefficient using a linear fit. Since the thermal expansion is more sensitive to the variation of temperature, a third-order polynomial function as used by Mei *et al* [76] has been employed for the fitting of the relationship between enthalpy and temperature. By taking the first derivative of this function, we obtained the heat capacity at different temperatures.

An MD simulation was also performed to estimate the heat of fusion. The box was firstly relaxed at 200 K for 200 ps to get a really stable initial configuration. Then it was heated

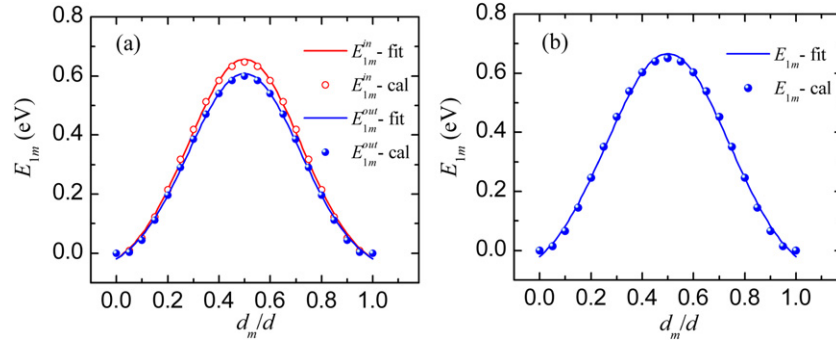


Figure 3. The calculated migration energies (circles) of a monovacancy and their fitted curves (solid lines) for Zr and Nb based on the present model. In the figure, d_m is the displacement in the moving path, d is the distance of the path. (a) Zr; (b) Nb.

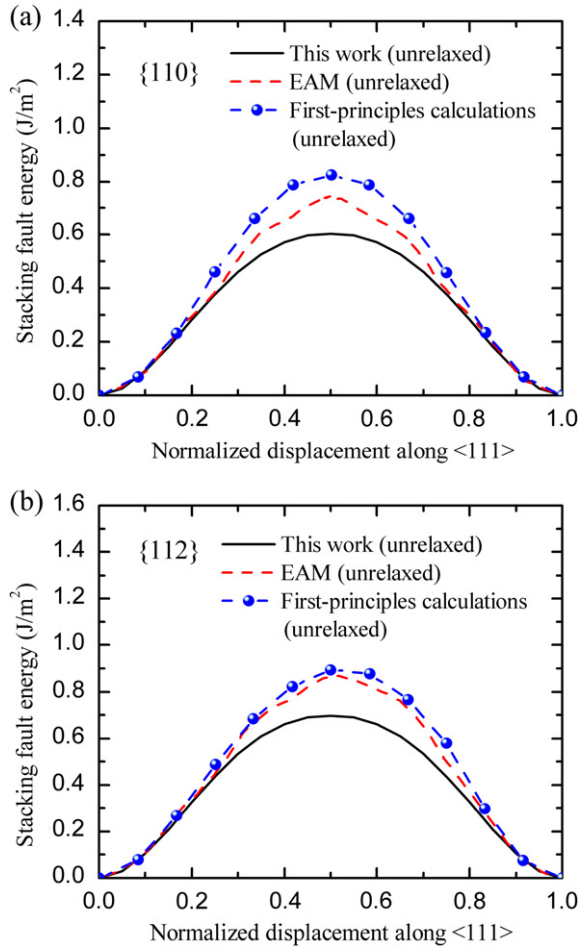


Figure 4. γ surface sections in the $\langle 111 \rangle$ direction for Nb. Results calculated from EAM and first-principles calculations are reproduced from figure 6 in [74].

from 200 K to a moderately high temperature (3000 K for Zr and 3500 K for Nb). All the conditions were set as those mentioned in the above section except that the heating rate is 2.5×10^{11} K s $^{-1}$. At 3000 K, the box was fully relaxed for 200 ps. Then it was cooled down to 300 K by the same strategy as was adopted for the heating process. The heats of fusion for Zr and Nb were estimated by comparing the variations of the enthalpy with temperature during the heating

and quenching process (as shown in figure 5). To maintain consistency with the previous work on MEAM [23, 38] and the TB-SMA model [27], the melting point, where energy jumps occur, was directly worked out from figure 5. Morris *et al* [77] pointed out that the melting point calculated by using the continuous heating scheme (the one-phase method) would overestimate the value by at least 500 K because of the heat hysteresis and heterogeneous nucleation problems. The values predicted in this work are at the upper boundary of the melting points for Zr and Nb. The coexisting-phases method [77] has been proved to be more precise in the determination of the melting point. In this work, we constructed an hcp supercell with $10 \times 10 \times 20 \times 4 = 8000$ atoms for Zr and a bcc supercell with $10 \times 10 \times 20 \times 2 = 4000$ atoms for Nb. The boxes were divided into two equal parts along the z axis. The upper part was firstly equilibrated at 3000 K for 200 000 steps to get a stable liquid configuration, and the lower part was equilibrated at 300 K. After that the coexisting-phases configuration was run for 200 000 steps at different temperatures under zero external pressure. Here the interval of each temperature is 20 K. In the equilibrating process, the solid–liquid interface will move to the liquid phase as the temperature is lower than melting point; otherwise, the interface will move to the solid phase. The interface would be stable at the middle of two phases at the melting point. Therefore, the melting point can be estimated by examining the final configurations of the coexisting phase simulated at different temperatures.

The thermodynamics properties calculated by using the present model, MEAM [24, 42] and TB-SMA [30], and experimental measurements obtained [39], have been listed in table 11. It is shown that, for Zr, the melting point calculated (by the one-phase method) and the heat of fusion in this work are comparable to those from MEAM-Kim [42], but the linear expansion coefficient and heat capacity are somewhat larger than those from MEAM-Kim [42] and experimental measurement [39]. Using coexisting-phases method, the predicted melting points are 1580 K for Zr. The melting point of Zr is underestimated by about 548 K using the present model, which may be due to the lack of consideration of the angularly dependent electron density distribution for Zr in this work. For Nb, the calculated heat of fusion, specific heat capacity and thermal expansion coefficient are in good agreement with those from the MEAM-2NN-Lee model [24]

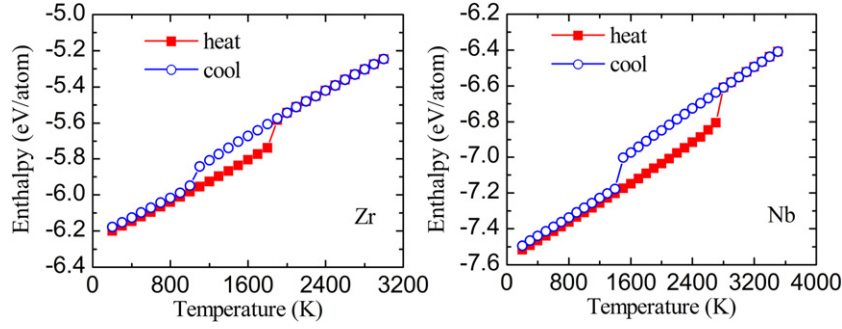


Figure 5. The enthalpy as a function of temperature for Zr and Nb calculated from molecular dynamics simulations.

Table 11. Some thermodynamics properties calculated on the basis of the present model and MEAM for Zr and Nb. The first line gives the experimental data [39], while the second line and third line give the properties calculated by using the present model and MEAM (Zr: MEAM-Kim, [42], Nb: MEAM-2NN-Lee, [24]), respectively. For the melting point, the fourth line gives results estimated from TB-SMA in [30], and the results in parentheses are the melting points calculated with the solid-liquid coexisting-phases method using the present model.

	Zr	Nb
Melting point (K)	2128	2750
	1850 (1580)	2750 (2380)
	1957	1900
	2100	3000
Heat of fusion (kJ mol ⁻¹)	21.00	30.0
	14.93	19.0
	16.09	13.5
Specific heat (J ⁻¹ mol ⁻¹ K ⁻¹ , 273–373 K)	26.4	24.9
	32.98	25.3
	25.7	26.1
Thermal expansion coefficient (1 × 10 ⁻⁶ K ⁻¹ , 273–373 K)	5.9	7.3
	11.4	6.9
	7.9	6.4

and experimental measurement [39]. Just like for Zr, the melting point predicted from the present potential for Nb is underestimated by 370 K. However, it seems that our prediction is better than that from the MEAM-2NN-Lee model [24]. On the basis of the above results, it is seen that our new n -body potential could be used to reproduce most of the basic thermodynamics properties for Zr and Nb reasonably well, and can be employed in molecular dynamics simulations.

3.5. Applications for alloys

In the above sections, we have proved the validity of the constructed potential for pure elements. The performance of this model for an alloy system will be demonstrated in the following section.

Since few experimental data are available for stable intermetallic compounds in the Zr–Nb system, it is difficult to fit the Zr–Nb cross-potential on the basis of experimental

data. In this work, we constructed some hypothetical Zr–Nb alloys with simple structures, and calculated their ground state properties by using first-principles methods. In order to get the real ground state energies of the alloys in different structures, series of volume–energy (V – E) relations were built. In these calculations, most of the conditions were set as those for pure element calculations. The V – E relations were fitted using the Rose universal EOS [31]

$$E(V) = -E_0(1 + a^* + 0.05a^{*3})e^{-a^*} \quad (12)$$

where $a^* = \sqrt{\frac{9B_0V_0}{E_c}}(\frac{V}{V_0} - 1)$, V is the volume, and E is the corresponding calculated total energy; B_0 , V_0 and E_0 are the bulk modulus, volume and energy at the ground state, respectively.

Because the energy reference states of the first-principles calculations and experimental cohesive energy are different, the calculated cohesive energies of alloys should be corrected to make them consistent [78]. The corrected cohesive energies of alloys were determined by using

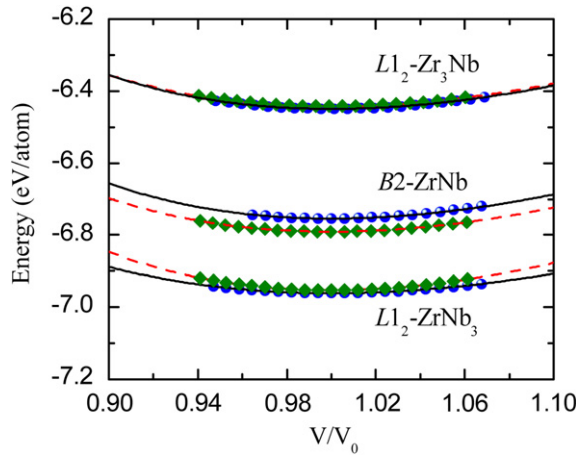
$$E_c^{A_xB_{1-x}} = E_0^{A_xB_{1-x}} + x(E_c^A - E_0^A) + (1-x)(E_c^B - E_0^B) \quad (13)$$

where $E_0^{A_xB_{1-x}}$, E_0^A and E_0^B are the static energies of A_xB_{1-x} compounds, A and B being elements, at 0 K according to first-principles calculations, respectively; E_c^A and E_c^B are the cohesive energies for pure elements. The EOS relations of B2-ZrNb, L1₂-Zr₃Nb and L1₂-ZrNb₃ are displayed in figure 6. All the results for 20 kinds of structures calculated by using the present model and the first-principles method are listed in table 12. For comparison, the results for B2-ZrNb, L1₂-Zr₃Nb and L1₂-ZrNb₃ calculated on the basis of the TB-SMA model [30] are also presented. From figure 6 and table 12, it is seen that the lattice constants, cohesive energies, bulk modulus and EOS reproduced by using the present potential are in good agreement with those from first-principles calculations and Li's work [30].

In this work, the constructed potential was also tested by calculating the formation energy of Zr_xNb_{1-x} random substitution solid solution with bcc and hcp types of structure. We constructed the supercell with 10 × 10 × 10 × 2 = 2000 atoms for bcc and 10 × 10 × 10 × 4 = 4000 atoms for hcp solid solutions. For bcc structure, the x , y and z axes are along [1 0 0], [0 1 0] and [0 0 1] crystal orientations, respectively. For hcp structure, the axes are along [1 0 0],

Table 12. The properties of Zr–Nb hypothetical alloys reproduced from the present model (first line), first-principles calculations (second line) and the TB-SMA model in [30] (third line). The alloys marked with asterisks (*) were included in the fittings.

	a (Å)	c (Å)	E_c (eV/atom)	B_0 (Mbar)		a (Å)	c (Å)	E_c (eV/atom)	B_0 (Mbar)
*C3-Zr ₂ Nb	5.61		4.86	0.72	*D0 ₃ -Zr ₃ Nb	7.10		6.49	1.07
	5.72		4.90	0.61		7.01		6.48	1.06
C7-Zr ₂ Nb	3.13	15.89	6.52	1.07	*D0 ₉ -Zr ₃ Nb	5.15		4.97	0.66
	3.09	15.67	6.50	1.08		5.18		5.10	0.55
C15-Zr ₂ Nb	8.12		6.36	1.72	D0 ₁₉ -Zr ₃ Nb	6.34	5.25	6.46	1.14
	8.04		6.20	1.04		6.29	5.16	6.45	1.05
*C32-Zr ₂ Nb	5.08	3.01	6.57	1.55	*L1 ₂ -Zr ₃ Nb	4.49		6.45	1.07
	4.98	2.96	6.52	1.16		4.45		6.44	1.06
						4.51		6.45	1.03
C _h -Zr ₂ Nb	5.25	5.77	6.26	1.11	*D0 ₃ -ZrNb ₃	6.78		7.12	1.57
	5.15	5.82	6.24	1.01		6.76		7.17	1.49
*C3-ZrNb ₂	5.17		4.88	0.50	*D0 ₉ -ZrNb ₃	4.88		5.07	1.04
	5.66		4.36	0.57		5.00		4.67	0.64
C7-ZrNb ₂	3.07	15.37	6.84	1.26	D0 ₁₉ -ZrNb ₃	6.08	5.10	6.95	0.80
	2.95	16.06	6.85	1.34		5.89	5.28	6.97	1.36
C15-ZrNb ₂	7.87		6.96	1.76	*L1 ₂ -ZrNb ₃	4.34		6.96	1.00
	7.88		7.08	1.41		4.30		6.95	1.44
						4.44		6.92	1.09
*C32-ZrNb ₂	4.92	2.75	6.85	1.48	*B1-ZrNb	5.47		6.03	1.00
	4.62	3.34	6.82	1.30		5.65		5.97	0.96
C _h -ZrNb ₂	4.63	7.73	6.06	0.75	B2-ZrNb*	3.48		6.69	1.16
	4.42	9.41	6.07	0.66		3.44		6.79	1.24
						3.57		6.77	1.38

**Figure 6.** The equations of state for B2-ZrNb, L1₂-Zr₂Nb and L1₂-ZrNb₂ fitted from the results calculated by using the present model and first-principles calculations. For each structure, solid circles (●) show results calculated by using the present model, and solid curves (—) are the corresponding fitted EOS curves; diamonds (◆) show results from first-principles calculations, and dashed curves (---) are the corresponding fitted EOS curves.

[0 $\sqrt{3}$ 0] and [0 0 c/a] crystal orientations, respectively. The random solid solution structures were generated by random substitution of the solvent atoms in the specific lattice for the solute atoms to get the desired concentration. For comparison, the energies of large scale Zr_xNb_{1-x} ($x = 0.25, 0.5$ and 0.75 ; for bcc: $20 \times 20 \times 20 \times 2 = 16\,000$ atoms; for hcp $20 \times 20 \times 20 \times 4 = 32\,000$ atoms) random solid solution supercells were also calculated. The formation energies were calculated by the energy minimization method through LAMMPS. Considering that no experimental data for the formation energy for random

solid solutions of the Zr–Nb system have been reported, we tested our model by comparing the formation energies with those obtained from first-principles calculations.

The special quasirandom structure (SQS) has been proved to provide a successful approach to mimicking random substitution solid solutions [79–82]. Previous publications have shown that the 16-atom SQS configurations are sufficient and can be used for mimicking the random bcc, fcc and hcp configurations beyond third-nearest neighbor shells [82]. In this work, we adopted 16-atom SQS configurations for the calculation of the formation energy by means of first-principles calculations. The cutoff energy was set to 400 eV and the k -point mesh grids for bcc and hcp were all generated as $9 \times 9 \times 9$, which ensures that the total energy was converged to less than 0.1 meV/atom. The supercells were relaxed only with the volume to preserve the symmetry, to avoid symmetry collapse happening. That means that the formation energies calculated by the SQS method in this work are considered as the upper bounds. In order to obtain the ground energies in the reference states, the calculated energies related to different volumes were also fitted using Rose's EOS [31].

The formation energy, ΔH_f , could be calculated by using

$$\Delta H_f(A_xB_{1-x}) = E_0^{A_xB_{1-x}} - xE_0^A - (1-x)E_0^B \quad (14)$$

where E_0^A , E_0^B and $E_0^{A_xB_{1-x}}$ are the ground energies of pure elements (A , B) and their solid solution at specific compositions, respectively. The structures of A , B and A_xB_{1-x} must be consistent. Furthermore, the formation energies of Zr–Nb were also calculated on the basis of the improved Miedema model proposed by Zhang *et al* (i.e. Miedema-ZSL-07) [83], which takes into account the effect of the atomic size difference between dissimilar metals to avoid underestimation

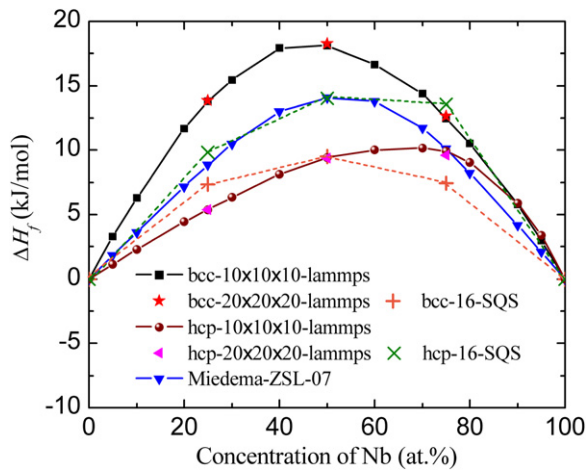


Figure 7. The formation energies of random solid solutions of Zr–Nb calculated by using the present model, the first-principles calculations based on the SQS model [81, 82] and the Miedema-ZSL-07 model [83].

of the formation energies. All the results calculated by using the present model, the first-principles calculations based on the SQS model [81, 82] and the Miedema-ZSL-07 model [83] are displayed in figure 7. It is seen that the differences in calculated formation energies between the $10 \times 10 \times 10$ and $20 \times 20 \times 20$ supercells are negligible, indicating that the size of the $10 \times 10 \times 10$ supercell is sufficient for avoiding the calculation uncertainties caused by different configurations. The trends predicted from the present model for the ΔH_f of the random solid solutions of bcc and hcp structure are consistent with those from first-principles calculations for ‘bcc-16-SQS’ and ‘hcp-16-SQS’, respectively, though some deviation is found. We also find that, in the high content range of Zr, the trends of ΔH_f for both bcc and hcp forms agree with those from the Miedema-ZSL-07 model. As Zr is decreased, the formation energy reaches a maximum value near the composition of 50%Zr–50%Nb for bcc solid solution and the Miedema-ZSL-07 Model calculation, but not for hcp solid solution. It is known that there exist two stable phases for Zr in the solid state: hcp for low temperature and bcc for high temperature. For Nb, only a bcc phase exists in the solid state. The mismatch between dissimilar atoms of a Zr–Nb solid solution would be less in a bcc structure than in an hcp structure. This may be one of the reasons for which the bcc solid solution and the Miedema-ZSL-07 model calculation results are in a consistent trend within a wide composition range. Besides this, as shown in figure 7, the formation energies of the Zr–Nb system calculated by using the present model are positive, which agrees with our first-principles calculations and the Miedema-ZSL-07 model.

On the basis of the above calculated results for hypothetical alloys and random substitution solid solutions, it is seen that the present potential can also be used for describing the dissimilar atom interactions for the Zr–Nb system.

4. Conclusions

- (1) In the framework of embedded-atom theory, an n -body potential for the Zr–Nb system was constructed. A ten-piece cubic polynomial function was introduced to characterize the cross-potential for dissimilar atoms. All the parameters of the new potential have been determined by fitting the basic physical properties obtained from experimental measurements and first-principles calculations for pure elements and some alloys.
- (2) By using the present potential, most static properties of Zr and Nb including the cohesive energy, lattice constants, elastic constants, bulk modulus (and its first derivative with pressure at 0 K), point defect properties, and formation energies of several low-index surfaces and stacking faults can be reproduced very well. Some thermodynamics properties like the thermal expansion coefficient, heat of fusion, specific heat capacity and melting point (estimated by the one-phase method) can be also be properly predicted through molecular dynamics simulations.
- (3) The ground state properties of hypothetical Zr–Nb alloys and the formation energies of random Zr–Nb solid solutions with lattices of bcc and hcp type were calculated by fitting the energy–volume relations to Rose’s EOS. Meanwhile, these properties for hypothetical Zr–Nb alloys with a random solid solution type of structure were also calculated by means of first-principles calculations based on SQS models and estimated using the Miedema-ZSL-07 model. Most of the calculation results attested to the Zr–Nb n -body potential that we constructed providing an effective description for the interaction between binary alloys composed of elements of hcp and bcc type.

Acknowledgment

The authors are grateful for financial support from the National Natural Science Foundation of China (Grants Nos 51071018 and 51271018).

References

- [1] Eagleson M 1994 *Concise Encyclopedia Chemistry* (Berlin: Walter de Gruyter) p 1199
- [2] Pérez R J and Massih A R 2007 *J. Nucl. Mater.* **360** 242
- [3] Bradley E R and Sabol G P 1996 *Zirconium in the Nuclear Industry: Eleventh International Symposium* (West Conshohocken, PA: ASTM) p 710
- [4] Sabol G P and Moan G D 2000 *Zirconium in the Nuclear Industry: Twelfth International Symposium* (West Conshohocken, PA: ASTM) p 505
- [5] Root J H and Fong R W L 1996 *J. Nucl. Mater.* **232** 75
- [6] Novikov V V, Markelov V A, Tselishchev A V, Kon’Kov V F, Sinelnikov L P and Panchenko V L 2006 *J. Nucl. Sci. Technol.* **43** 991
- [7] Pythian W J, Stoller R E, Foreman A J E, Calder A F and Bacon D J 1995 *J. Nucl. Mater.* **223** 245
- [8] Foreman A J E, Pythian W J and English C A 1992 *Phil. Mag.* **66** 671

- [9] Shim J-H, Lee H-J and Wirth B D 2006 *J. Nucl. Mater.* **351** 56
- [10] Tikhonchev M, Svetukhin V, Kadochkin A and Gaganidze E 2009 *J. Nucl. Mater.* **395** 50
- [11] Finnis M W and Sinclair J E 1984 *Phil. Mag. A* **50** 45
- [12] Ackland G J, Wooding S J and Bacon D J 1995 *Phil. Mag. A* **71** 553
- [13] Cleri F and Rosato V 1993 *Phys. Rev. B* **48** 22
- [14] Johnson R A 1988 *Phys. Rev. B* **37** 3924
- [15] Oh D J and Johnson R A 1988 *J. Mater. Res.* **3** 471
- [16] Johnson R A and Oh D J 1989 *J. Mater. Res.* **4** 1195
- [17] Zhang R F, Kong Y and Liu B X 2005 *Phys. Rev. B* **71** 214102
- [18] Johnson R A 1989 *Phys. Rev. B* **39** 12554
- [19] Cai J and Ye Y 1996 *Phys. Rev. B* **54** 8398
- [20] Wadley H N G, Zhou X, Johnson R A and Neurock M 2001 *Prog. Mater. Sci.* **46** 329
- [21] Zhou X W, Wadley H N G, Filhol J S and Neurock M N 2004 *Phys. Rev. B* **69** 035402
- [22] Zhang B and Ouyang Y 1993 *Phys. Rev. B* **48** 3022
- [23] Baskes M I and Johnson R A 1994 *Modelling Simul. Mater. Sci. Eng.* **2** 147
- [24] Lee B-J, Baskes M I, Kim H and Cho Y K 2001 *Phys. Rev. B* **64** 184102
- [25] Lee B-J, Shim J-H and Baskes M I 2003 *Phys. Rev. B* **68** 144112
- [26] Mishin Y, Mehl M J and Papaconstantopoulos D A 2005 *Acta Mater.* **53** 4029
- [27] Mishin Y, Asta M and Li J 2010 *Acta Mater.* **58** 1117
- [28] Sa I and Lee B J 2008 *Scr. Mater.* **59** 595
- [29] Gong H R, Kong L T, Lai W S and Liu B X 2002 *Phys. Rev. B* **66** 104204
- [30] Li J H, Dai Y, Dai X D, Wang T L and Liu B X 2008 *Comput. Mater. Sci.* **43** 1207
- [31] Rose J H, Smith J R, Guinea F and Ferrante J 1984 *Phys. Rev. B* **29** 2963
- [32] Willaime F and Massobrio C 1991 *Phys. Rev. B* **43** 11653
- [33] Kresse G and Furthmüller J 1996 *Phys. Rev. B* **54** 11169
- [34] Kresse G and Joubert D 1999 *Phys. Rev. B* **59** 1758
- [35] Vanderbilt D 1990 *Phys. Rev. B* **41** 7892
- [36] Perdew J P, Chevary J A, Vosko S H, Jackson K A, Pederson M R, Singh D J and Fiolhais C 1992 *Phys. Rev. B* **46** 6671
- [37] Monkhorst H J and Pack J D 1976 *Phys. Rev. B* **13** 5188
- [38] Plimpton S 1995 *J. Comput. Phys.* **117** 1
- [39] Lide D R 2009 *CRC Handbook of Chemistry and Physics: A Ready-Reference Book of Chemical and Physical Data* (Boca Raton, FL: CRC Press)
- [40] Nôse S 1984 *J. Chem. Phys.* **81** 511
- [41] Hoover W G 1985 *Phys. Rev. A* **31** 1695
- [42] Kim Y-M, Lee B-J and Baskes M I 2006 *Phys. Rev. B* **74** 014101
- [43] Wang Y, Curtarolo S, Jiang C, Arroyave R, Wang T, Ceder G, Chen L Q and Liu Z K 2004 *Calphad* **28** 79
- [44] Shang S L, Saengdeejing A, Mei Z G, Kim D E, Zhang H, Ganeshan S, Wang Y and Liu Z K 2010 *Comput. Mater. Sci.* **48** 813
- [45] Le Bacq O, Willaime F and Pasturel A 1999 *Phys. Rev. B* **59** 8508
- [46] Baskes M I 1992 *Phys. Rev. B* **46** 2727
- [47] Kittel C 2005 *Introduction to Solid State Physics* (New York: Wiley)
- [48] Simmons G and Wang H 1971 *Single Crystal Elastic Constants and Calculated Aggregate Properties: A Handbook* (Cambridge, MA: MIT Press)
- [49] De Boer F R, Boom R, Mattens M C M, Miedema A R and Nissen A K 1988 *Cohesion in Metals: Transition Metal Alloys* (Amsterdam: North-Holland, Elsevier)
- [50] Hood G M 1986 *J. Nucl. Mater.* **139** 179
- [51] Korhonen T, Puska M J and Nieminen R M 1995 *Phys. Rev. B* **51** 9526
- [52] Korzhavyi P A, Abrikosov I A, Johansson B, Ruban A V and Skriver H L 1999 *Phys. Rev. B* **59** 11693
- [53] Söderlind P, Yang L H, Moriarty J A and Wills J M 2000 *Phys. Rev. B* **61** 2579
- [54] Takamura J, Doyama M and Kiritani M 1982 *Point Defects and Defect Interactions in Metals* (Tokyo: University of Tokyo Press) p 533
- [55] Ullmaier H, Ehrhart P, Jung P and Schultz H 1991 *Atomic Defects in Metals* (Berlin: Springer)
- [56] Hu W, Zhang B, Huang B, Gao F and Bacon D J 2001 *J. Phys.: Condens. Matter* **13** 1193
- [57] Neely H H 1970 *Radiat. Eff.* **3** 189
- [58] Hood G M, Schultz R J and Jackman J A 1984 *J. Nucl. Mater.* **126** 79
- [59] Hood G M and Schultz R J 1988 *J. Nucl. Mater.* **151** 172–80
- [60] Matsuura N, Hood G M and Zou H 1996 *J. Nucl. Mater.* **238** 260
- [61] Hu W Y, Shu X L and Zhang B W 2002 *Comput. Mater. Sci.* **23** 175
- [62] Gale W F and Totemeier T C 2004 *Smithells Metals Reference Book* 8th edn (Oxford: Elsevier)
- [63] Tyson W R and Miller W A 1977 *Surf. Sci.* **62** 267
- [64] Mezey L Z and Gibber J 1982 *Japan. J. Appl. Phys.* **21** 1569
- [65] Sundquist B E 1964 *Acta Metall.* **12** 67
- [66] Grenga H E and Kumar R 1976 *Surf. Sci.* **61** 283
- [67] Wang W Y, Shang S L, Wang Y, Darling K A, Mathaudhu S N, Hui X D and Liu Z K 2012 *Chem. Phys. Lett.* **551** 121
- [68] Wu X, Wang R and Wang S 2010 *Appl. Surf. Sci.* **256** 3409
- [69] Legrand P B 1984 *Phil. Mag. B* **49** 171
- [70] Dai Y, Li J H and Liu B X 2009 *J. Phys.: Condens. Matter* **21** 385402
- [71] Vitek V 1968 *Phil. Mag.* **18** 773–86
- [72] Devlin J F 1981 *J. Phys. F: Met. Phys.* **11** 2497
- [73] Yan J-A, Wang C-Y and Wang S-Y 2004 *Phys. Rev. B* **70** 174105
- [74] Fellingner M R, Park H and Wilkins J W 2010 *Phys. Rev. B* **81** 144119
- [75] Duesbery M and Vitek V 1998 *Acta Mater.* **46** 1481
- [76] Mei J, Davenport J W and Fernando G W 1991 *Phys. Rev. B* **43** 4653
- [77] Morris J R, Wang C Z, Ho K M and Chan C T 1994 *Phys. Rev. B* **49** 3109
- [78] Li J H, Dai X D, Liang S H, Tai K P, Kong Y and Liu B X 2008 *Phys. Rep.* **455** 1
- [79] Zunger A, Wei S H, Ferreira L G and Bernard J E 1990 *Phys. Rev. Lett.* **65** 353
- [80] Wei S H, Ferreira L G, Bernard J E and Zunger A 1990 *Phys. Rev. B* **42** 9622
- [81] Jiang C, Wolverton C, Sofo J, Chen L-Q and Liu Z-K 2004 *Phys. Rev. B* **69** 214202
- [82] Shin D, Arroyave R, Liu Z-K and Van de Walle A 2006 *Phys. Rev. B* **74** 024204
- [83] Zhang R F, Sheng S H and Liu B X 2007 *Chem. Phys. Lett.* **442** 511